Solar Energy Materials & Solar Cells 257 (2023) 112358

Contents lists available at ScienceDirect

Solar Energy Materials and Solar Cells

journal homepage: www.elsevier.com/locate/solmat

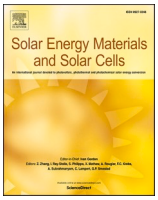

Four failure modes in silicon heterojunction glass-backsheet modules

Chandany Sen *, Haoran Wang, Xinyuan Wu, Muhammad Umair Khan, Catherine Chan, Malcolm Abbott, Bram Hoex

School of Photovoltaic and Renewable Energy Engineering, University of New South Wales, Sydney, NSW, 2052, Australia

ARTICLE INFO

Keywords:
Silicon heterojunction solar cells
Damp heat
Failure mode
Humidity-induced degradation
Ethylene vinyl acetate
Glass-backsheet modules

ABSTRACT

Silicon heterojunction technology (HJT) is expected to gain a significant market share in the near future. For HJT to deliver a low levelized cost of electricity (LCOE), it needs to have a high initial efficiency and degrade less than 0.5% relative per year. This work investigates damp heat-induced failure modes in silicon HJT glass-backsheet modules. Four unique failure modes are identified after damp heat (DH) testing: point failure (Type-1); failure around the interconnected regions of the busbars and ribbon wires (Type-2); failure between the busbars (Type-3); and failure at/on the interconnected regions of busbars and ribbon wires (Type-4). The Type-1 failure mode is likely caused by a chemical reaction between surface contaminants (introduced to the cells during handling or characterization before encapsulation) and moisture that increase charge carrier recombination and lead to a loss in maximum power (P_{max}) of up to 40%$_{rel}$ in this study. Type-2 and Type-3 failure modes cause P_{max} losses of ~5%$_{rel}$ and 50%$_{rel}$, respectively, in this study and can appear due to exposure to soldering flux used for connecting the ribbon wires and busbars. Finally, the Type-4 failure mode causes a P_{max} loss of ~16%$_{rel}$ in this study after the DH test. The evidence suggests that this failure mode is likely due to the interaction of acetic acid, generated from a reaction between the encapsulation material and moisture, ribbon wires, and silver paste (busbars), resulting in recombination loss. We believe these failure modes must be well understood and mitigated at preferably the solar cell level to ensure that HJT can meet its LCOE potential.

1. Introduction

For economical and sustainability reasons, photovoltaic (PV) modules should continue to output over 80% of their initial performance for at least 25 years, and ideally 50 years [1]. Silicon heterojunction (HJT) solar cells have been recognized as one of the most prominent technologies to improve silicon solar cell power generation, and they currently hold the silicon world record efficiency of 26.81% [2]. However, HJT modules can suffer from damp-heat (DH) or humidity-induced degradation when encapsulated with ethyl-vinyl acetate (EVA) between a front glass and rear backsheet structure as is commonly used for the passivated emitter, and rear cell (PERC) and tunnel oxide passivated contact (TOPCon) solar cells [3–5]. The DH test causes a significant increase in both series resistance and recombination, resulting in severe power loss [3–6]. To avoid this, current-generation HJT modules typically use polyolefin elastomer (POE) instead of EVA and glass sheets for both the front and rear sides, resulting in a relatively stable module [3,7]. However, these modules have a high risk of breakages, increased module weight, reduced yield generation, and, most importantly, increased manufacturing costs [8]. A glass-backsheet module with EVA encapsulation would be preferred if humidity-induced failures could be prevented. To enable this, it is critical to understand the different types of failure and their root causes. Unlike the PERC technology, where humidity-induced failure modes and root causes have been broadly studied and well understood, there is only limited work published for the HJT cell technology. A cell-level testing standard that was developed for PERC [9] is unsuitable for HJT cells due to its severe impact on the indium tin oxide (ITO) layers. However, cell-level testing is crucial as it allows more advanced characterization which enables quicker pinpointing of the cause(s) of degradation. This work aims to understand the overall damp-heat failure modes in HJT glass-backsheet modules, localize the failed regions, replicate similar failure modes at the cell-level, and suggest the root cause of each failure mode. These findings will help in developing solutions at the cell level to protect cells from failure, which we believe is essential for HJT to meet its full levelized cost of electricity (LCOE) potential.

* Corresponding author.
E-mail address: chandany.sen@unsw.edu.au (C. Sen).

https://doi.org/10.1016/j.solmat.2023.112358
Received 1 December 2022; Received in revised form 30 March 2023; Accepted 29 April 2023
Available online 4 May 2023

2. Experiment

Bifacial half-cut n-type silicon HJT solar cells and partly processed cell precursors with a size of 182 mm (L) × 91 mm (W) sourced from industrial production lines were used in this work. All samples were split into 3 groups: 1) modules with encapsulated cells, 2) modules with encapsulated cell precursors (HJT lifetime precursors with busbars connected to ribbon wires either on the front or on the rear), and 3) non-encapsulated cells. All samples featured an n-type wafer, intrinsic hydrogenated amorphous silicon (i-a-Si:H) passivation layers on both sides, and phosphorus-doped (n-a-Si:H) and boron-doped (p-a-Si:H) hydrogenated amorphous silicon layers on the front and rear sides, respectively, followed by indium-doped tin oxide (ITO) layer deposited on both sides. It is noted that due to the high cost and the scarcity of indium, alternatives to ITO are investigated for HJT solar cells [10–12]. A screen-printed H-pattern silver grid was printed on both sides of cells in Groups 1 and 3, the schematic diagram of these cells can be seen in Fig. 1 (a). For Group 2, one sample had screen-printed busbars connected with ribbon wires on the front side (Group 2-a), while another had screen-printed busbars connected with ribbon wires on the rear side (Group 2-b). All cells in Group 1 and some in Group 3 had tabbing and ribbon wires connected to busbars on both the front and rear sides using a standard industrial soldering process. EVA encapsulation was used for both the front and rear sides, followed by glass on the front and backsheet on the rear side for samples in Groups 1 and 2, while for the cells in Group 3, no EVA, glass, and backsheet were used (non-encapsulated). Note that all mini-modules with encapsulated cells (Group 1) and cell precursors (Group 2) were fabricated at an industrial facility. All soldering processes to connect ribbon wires with busbars were also done at the industrial sites.

The non-encapsulated cells in Group 3 were used to investigate the root cause of each failure mode observed in modules. These cells were divided into 5 sub-groups: a) non-cleaned, b) pre-cleaned, c) flux between busbars, d) flux on busbars, and e) acetic acid on busbars. Cells in sub-groups (c-e) were laser cleaved into 50 mm (L) × 91 mm (W) tokens after being connected to ribbon/tabbing wires due to limited cell availability. Subsequently, cells in the sub-groups (b-e) were cleaned with deionized (DI) water and dried by blowing nitrogen (N_2) on both sides before the subsequent processes to minimize surface contamination (potentially introduced from contaminated gloves, placed on contaminated stages for characterization, etc.). Cells in sub-groups (c) and (d) were exposed to soldering flux (both sides) between and on the interconnected regions of the busbars and ribbon wires, respectively, before the damp heat (DH) test to study the role of soldering flux on the failure. The cell in sub-group (e) was exposed to acetic acid 35% on the interconnected region of busbars and ribbon wires to understand its impact on the degradation behavior.

All samples in Groups 1, 2 and some cells in Group 3 (3-a and 3-b) then underwent a DH test at 85 °C and 85% relative humidity (RH) between 500 h and 4000 h, depending on the groups to determine failure modes after the DH test. Some cells in Group 3 (3-c, 3-d, 3-e) were DH tested with conditions of 100 °C and 85% RH to accelerate the test; see Fig. 1 for the detailed experimental flow diagram and an example image of one of the mini-modules used in this work (Group 1). Note that prior to the introduction of humidity, all samples were preheated in the chamber for 20 min to prevent condensation of water on samples.

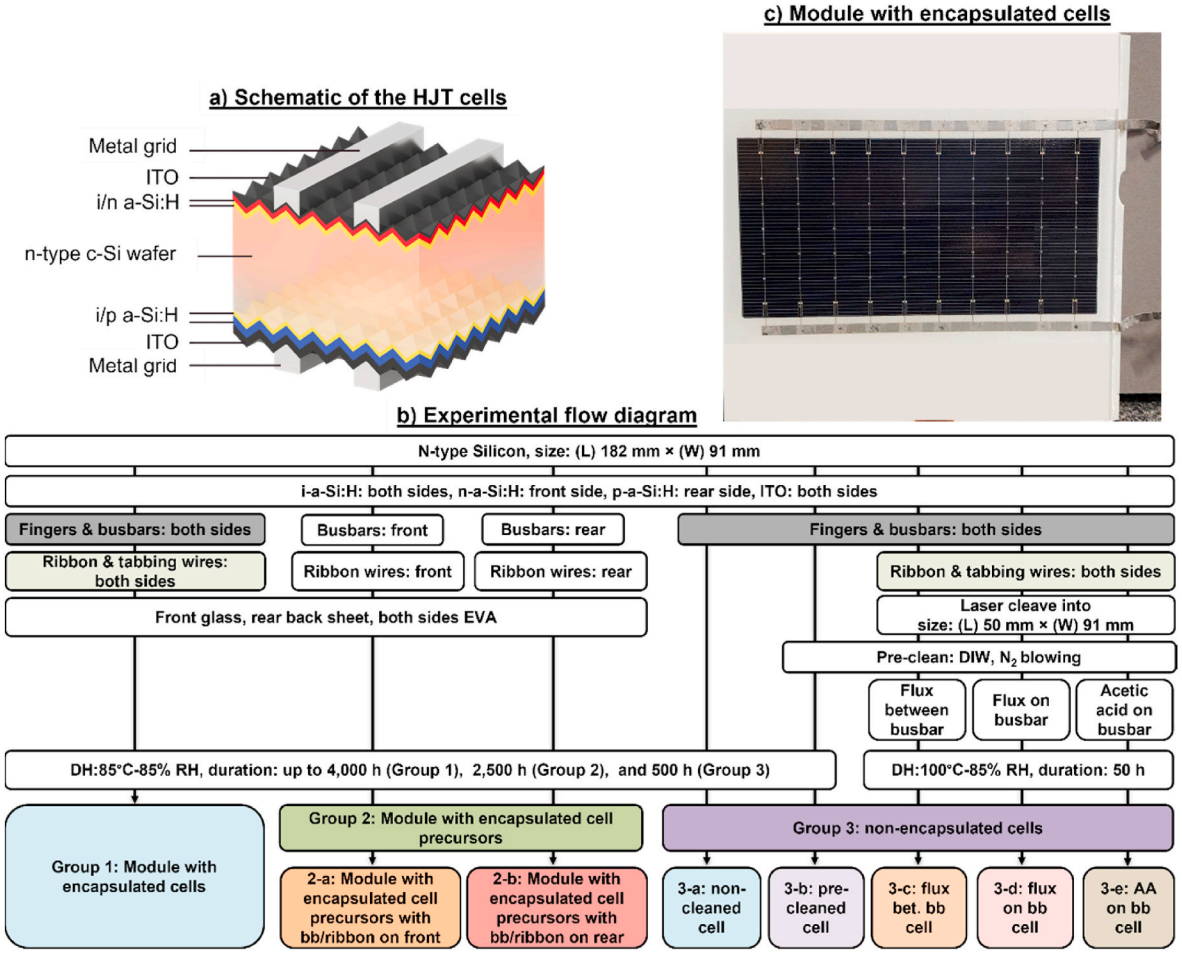

Fig. 1. a) Schematic of HJT cells, b) experimental flow diagram (bet. means between, bb means busbars, and AA means acetic acid), and c) photo of a module with encapsulated cell (show as an example of Group 1 sample used in this work).

The current-voltage (I–V) measurements were performed for Group 1 at standard testing conditions at the initial state and after incremental steps during the DH test using a commercial module flash tester (Eternalsun Spire, Spi-Sun Simulator™ 5600SLP Blue System) tool and Group 3 was tested using a commercial solar cell analysis tool (pv-tools LOANA). For all samples, the line-scan open circuit photoluminescence (PL_{LS}), electroluminescence (EL_{LS}), and series resistance (R_s) images were captured using a BTi-M1 luminescence line-scan system before and after the DH test.

Line-scan open circuit PL_{LS} is a contactless qualitative method that can distinguish series resistance defects from recombination defects in solar cells [13–15]. Line-scan PL_{LS} imaging is performed by restricting the camera field of view to a thin line spanning the width of a sample and localizing photoexcitation within this line. Individual line images are continuously acquired in sync with the sample motion, enabling on-the-fly imaging. The final image is produced by combining the acquired line images within the sample. As only a fraction of the cell area is illuminated at one time, there is a lateral current flow between the illuminated and nonilluminated regions. This means that the resulting PL_{LS} intensity is not only determined by the local minority carrier lifetime but also by the local R_S [13–15]. In PL_{LS}, regions with relatively high R_s will show a higher PL_{LS} intensity than areas with relatively low R_s [13–15].

3. Results and discussion

Four failure modes were identified in the modules with encapsulated cells (Group 1) after DH testing, leading to P_{max} loss ranging from 5 to 50%$_{rel}$ depending on the failure mode. These failure modes appear as different darkened features in the EL_{LS} images of Fig. 2: Type-1 darkened in localized points; Type-2 developed darkening around the interconnection of busbars and ribbon wires; Type-3 became very dark between the interconnected regions of busbars and ribbon wires; and Type-4 darkened at/on the interconnected region of busbars and ribbon wires. The details of each failure mode will be discussed in the subsequent sections.

3.1. Type-1 failure mode: point degradation

Fig. 3 shows the relative changes in I–V parameters and EL_{LS}, PL_{LS}, and R_s images taken before and after DH testing of modules with encapsulated HJT cells (Group 1) with the Type-1 failure mode. After 1000 h of DH testing, P_{max} reduced by ~10%$_{rel}$, which increased to ~40%$_{rel}$ after 4000 h of DH testing. The saturation current density for both the n = 1 and n = 2 diode (J_{01} and J_{02}) increased ≥3 orders of magnitude, respectively, after 1000 h of DH testing and further increased with continued DH conditions, leading to a significant drop in open circuit voltage (V_{OC}) of ~10%$_{rel}$. This is consistent with results reported by Karas et al. where V_{OC} degraded significantly after the DH test, leading to a severe drop in P_{max} [3]. In addition, a substantial drop in short circuit current (J_{SC}) of ~30%$_{rel}$ was potentially due to the degradation of the ITO layers caused by the contaminants since there was no encapsulant discolouration observed (data not shown here) [16], and resulted in ~40%$_{rel}$ reduction of P_{max}. The initial PL_{LS} and EL_{LS} images were relatively clean; however, after 1000 h of DH testing, many dark spots randomly appeared in the modules, reducing luminescence intensity (both PL_{LS} and EL_{LS}). Prolonging the DH test duration to 4000 h, a failure appeared in the center of the cells in the shape of a dark rectangle, in addition to the random dark spot failures. Further investigation is required to determine whether this is a new failure mode or an extended failure of the Type-1 failure mode. The R_s images showed an overall improvement after the DH test, even in failed regions, and were consistent with the one-sun I–V results (R_s decreased by ~30%$_{rel}$).

3.2. Type-2 failure mode: degradation around the interconnection of busbars and ribbon wires

Fig. 4 (a) shows the changes in the I–V parameters, and Fig. 4 (b) shows the EL_{LS}, PL_{LS}, and R_s images of modules with encapsulated HJT cells with the Type-2 failure mode. After 1500 h of DH testing, this failure mode caused P_{max} to drop ~5%$_{rel}$ with R_s increase ~30%$_{rel}$ as the primary loss. This failure mode caused a decrease in $EL_{LS,}$ but an increase in PL_{LS} counts around the interconnected regions of busbars and ribbon wires, primarily because carriers were unable or less likely to be electrically extracted from this region, leading to an increase in R_s (see R_s images) [15]. Fig. 4 (c) illustrates the changes in PL_{LS} before and after 1500 h of DH testing and the differential PL_{LS} images (DH 1500 h minus initial) of modules with encapsulated cell precursors (Group 2) with partial metallization (only busbars and ribbon wires) on the front only, and rear only. No significant changes in PL_{LS} intensities were observed in the module with encapsulated cell precursors with partial metallization on the front side (Group 2-a). However, the Type-2 failure mode was observed in the module with encapsulated cell precursors with partial metallization on the rear (Group 2-b). There was a substantial increase in the PL_{LS} counts around the interconnected regions of busbars and ribbon wires, which was better visualized in the PL_{LS} subtracted image (bright regions), indicating an increase in R_s in those regions [15]. These results suggest that the Type-2 failure mode mainly occurred on the rear side, where moisture permeated the modules via the backsheet and interacted with ribbon wires, soldering flux, Ag paste (busbars), and ITO layer leading to corrosion [17]. Note that failure around the interconnection of busbars and ribbon wires (Type-2 failure mode) is one of the most common failure modes that has also been observed in glass-backsheet modules fabricated using other cell technologies [18, 19].

3.3. Type-3 failure mode: degradation between the interconnection of busbars and ribbon wires

Fig. 5 illustrates the changes in the I–V parameters and EL_{LS}, PL_{LS},

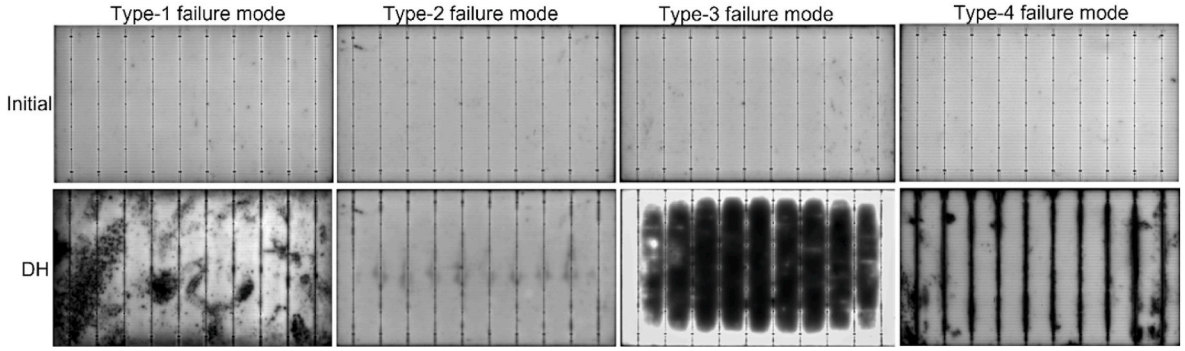

Fig. 2. EL_{LS} images of modules with encapsulated cells (Group1) before (initial) and after DH testing show four failure modes.

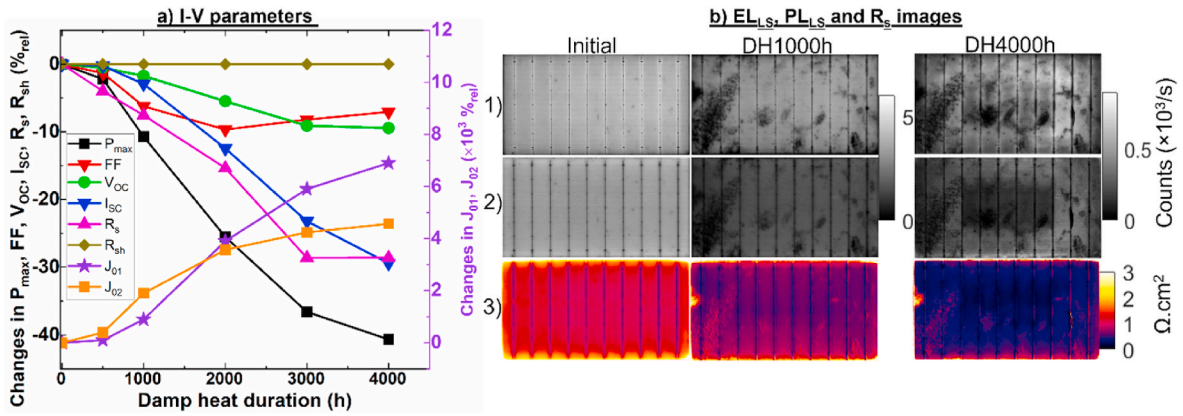

Fig. 3. Changes in a) I–V parameters and b) EL_{LS} (1), PL_{LS} (2), and R_s (3) images of modules with encapsulated cells that show Type-1 failure mode after DH testing.

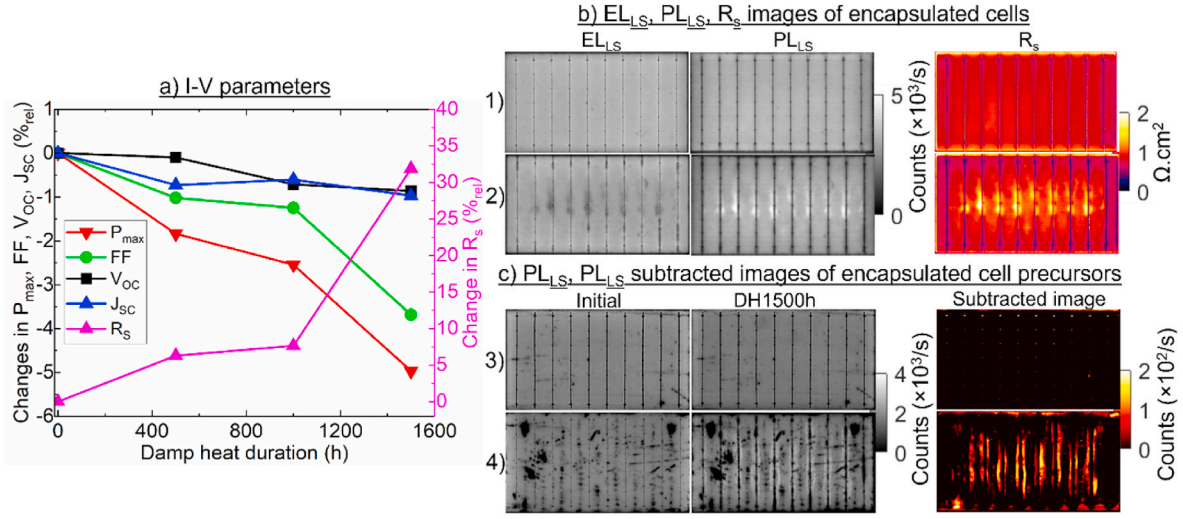

Fig. 4. Changes in a) I–V parameters and b) EL_{LS}, PL_{LS}, and R_s images at 1) initial, 2) DH1500h of modules with encapsulated cells that showed Type-2 failure mode after DH testing. c) changes in PL_{LS} images before and after 1500 h of DH testing and PL_{LS} subtracted images (DH1500h minus initial) of the modules with encapsulated HJT cell precursors with partial metallization (busbars and ribbon wires), 3) on the front (Group 2-a) and 4) on the rear (Group 2-b), showing Type-2 failure mode occurred on the rear side.

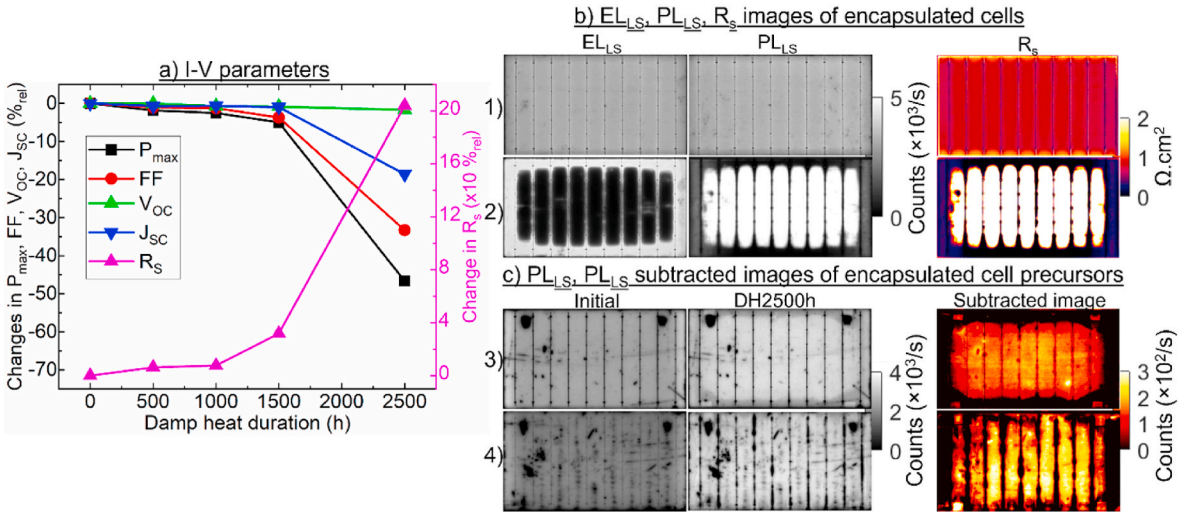

Fig. 5. Changes in a) I–V parameters and b) EL_{LS}, PL_{LS}, and R_s images at 1) initial, 2) DH2500h of modules with encapsulated HJT cells that showed Type-3 failure mode after DH testing. c) change in PL_{LS} images before and after 2500 h of DH testing and PL_{LS} subtracted images (DH2500h minus initial) of the modules with encapsulated cell precursors with partial metallization (busbars and ribbon wires) 3) on the front (Group 2-a) and 4) on the rear (Group 2-b), showing Type-3 failure mode occurred on both sides.

and R_s images of modules with encapsulated cells that show Type-3 failure mode after the DH test. The Type-3 failure mode was the most severe failure mode that caused a significant increase in R_s (~200%$_{rel}$), leading to a massive decrease in P_{max} of up to ~50%$_{rel}$ after 2500 h of DH testing. This failure mode was the long-term development of the Type-2 failure mode. It decreased EL_{LS}, but increased PL_{LS} intensities in the areas between the interconnection of busbars and ribbon wires due to a significant increase in R_s; therefore, the carriers could not be extracted [15]. This failure mode was also observed in the modules from Group 2 with encapsulated cell precursors that were only partially metallized (busbars, ribbon wires) on either the front or rear side, see Fig. 5 (c). After the DH test, there was a substantial increase in the PL_{LS} counts of these modules (the bright region in PL_{LS} subtracted images), indicating an increase in R_s of these modules (with HJT cell precursors). Note that no fingers were printed on these HJT cell precursors, suggesting that the Type-3 failure mode in this study was likely related to a failure of the ITO layer, for example, by corrosion.

3.4. Type-4 failure mode: degradation at/on the interconnection of busbars and ribbon wires

Changes in the I–V parameters and EL_{LS}, PL_{LS}, and R_s images of modules with encapsulated HJT cells that show Type-4 failure mode after the DH test can be found in Fig. 6. This failure mode reduced P_{max} ~16%$_{rel}$ after 4000 h of DH testing. Type-4 failure mode caused an increase in R_s of ~8%$_{rel}$ and some recombination loss, resulting in V_{OC} and I_{SC} dropping by ~4%$_{rel}$ after 4000 h of DH testing. The I–V data showed consistent results with changes in EL_{LS} and PL_{LS} (decreased intensity) on the interconnected regions of busbars and ribbon wires, suggesting increased recombination in the failed regions. R_s images show a slight increase in the failed regions but some improvement in the non-failed areas. The explanation for this improvement remains unclear; a more detailed study is required to explain this observation. Changes in PL_{LS} and PL_{LS} subtracted images (initial minus DH2500h) of the modules with encapsulated HJT cell precursors can be seen in Fig. 6 (c). The Type-4 failure mode was mainly observed in the module with HJT cell precursors with partial metallization on the rear side (Group 2-b, bright regions in PL_{LS} subtracted images, indicating a loss in PL intensity in the failed region). No Type-4 failure mode was observed in the module with partial metallization on the front side (Group 2-a, PL counts on the interconnected regions remained almost unchanged). These results imply that Type-4 failure primarily occurred on the rear side, where moisture penetrated the modules via the backsheet and reacted with ribbon wires, acetic acid (generated from EVA), Ag paste (busbars), and ITO layer leading to recombination loss.

3.5. Root causes of each failure mode

To further understand the root causes of each failure mode, DH testing was also carried out on the non-encapsulated cells (Group 3). Fig. 7 shows the changes in P_{max}, V_{OC}, and PL_{LS} images of non-encapsulated cells that were cleaned (Group 3-b) and not cleaned (Group 3-a) prior to the DH test [more detail of these groups can be seen in Fig. 1 (b)]. After 500 h of DH testing (85 °C, 85% RH), no changes in P_{max}, V_{OC}, and PL_{LS} images were observed in the cell cleaned before the DH test. However, the P_{max} of non-encapsulated cells that were not cleaned prior to the DH test dropped by ~20%$_{rel}$, and V_{OC} decreased by 7%$_{rel}$,.In addition, there were many localized point failures that occurred in the PL_{LS} image after DH testing, particularly at the edge of the cells where they were touched/handled (potentially using contaminated gloves in our case). The failure behavior in the non-cleaned cell after DH testing was similar to the Type-1 failure mode observed in the glass-backsheet module with encapsulated cells (Group 1), suggesting that Type-1 failure mode is potentially caused by surface contamination. This contamination was probably accidently introduced during handling (touching the surface of the cells with bare fingers or contaminated gloves/handlers) and/or characterization (placing the cells on potentially contaminated characterization stages) before module encapsulation. These contaminants may chemically interact with moisture and cause recombination, leading to a severe power loss after the DH test. Note that J_{01} and J_{02} of non-cleaned cells with Type-1 failure mode also increased after the DH test (data not shown), further implying that recombination loss was mainly due to an increase in surface recombination [20,21]. The exact type of contamination, or how it reacted with moisture leading to an increase in recombination, is still unclear. However, these results show that this contamination can be minimized by handling bare cells with fresh/clean gloves, cleaning characterization stages before using, and/or cleaning bare cells with DIW, followed by N_2 drying prior to module encapsulation and DH testing. This result highlights that surface contamination is very harmful to HJT cells, mainly when exposed to moisture at elevated temperatures; therefore, careful attention should be paid to handling in HJT manufacturing. Note that in high-volume solar module manufacturing, handling is fully automated. However, it should be assured that all handlers are clean to avoid

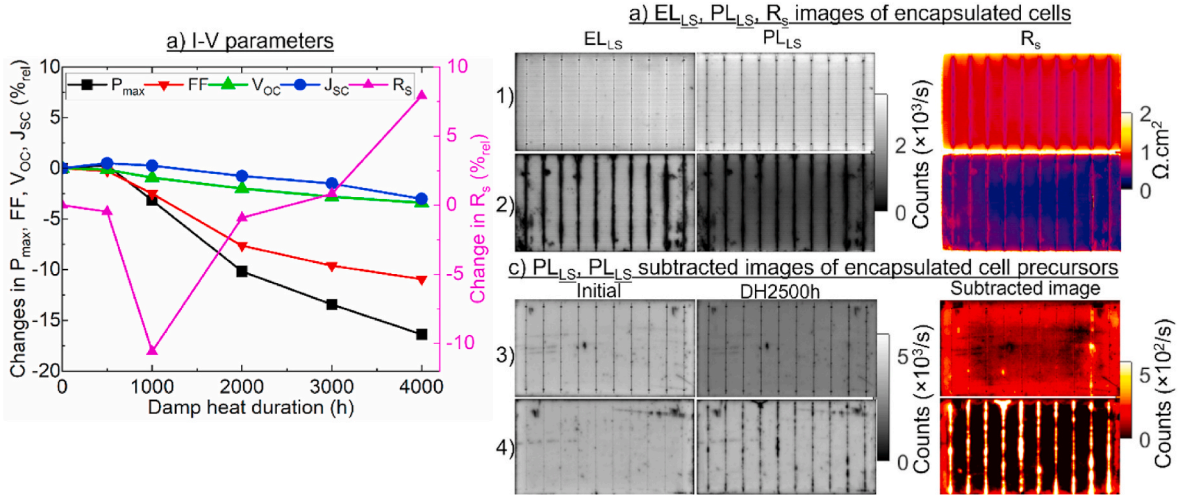

Fig. 6. Changes in a) I–V parameters and b) EL_{LS}, PL_{LS}, and R_s images 1) initial, 2) DH4000h of modules with encapsulated cells (Group 1) that showed Type-4 failure mode after DH testing. c) changes in PL_{LS} images before and after 2500 h of DH testing and PL_{LS} subtracted images (Initial minus DH2500h) of the modules with encapsulated cell precursors with partial metallization (busbars and ribbon wires) 3) on the front (Group 2-a) and 4) on the rear (Group 2-b), showing Type-4 failure mode occurred primarily on the rear side.

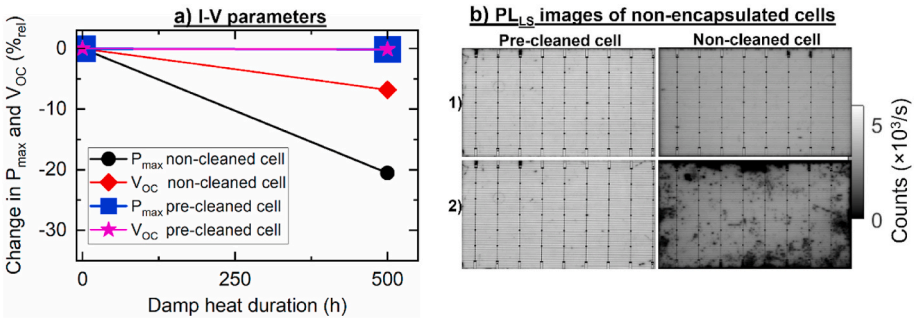

Fig. 7. Changes in a) I–V parameters and b) PL_{LS} images 1) initial, 2) DH500h of non-encapsulated HJT cells that were not cleaned (Group 3-a) and cleaned with DIW, followed by N_2 drying (Group 3-b) before DH testing. The non-clean cell shows a Type-1 failure after DH testing.

contamination of the solar cell precursors.

Unlike Type-1 failure mode, Type-2, Type-3, and Type-4 failure modes were only observed in the encapsulated cells but not in the non-encapsulated (both pre-clean and non-cleaned cells) that directly underwent the DH test. However, Type-2, Type-3, and Type-4 failure modes were observed in the non-encapsulated cells exposed to soldering flux (Groups 3-c and 3-d) and acetic acid (Group 3-e) on/between interconnected regions of busbars and ribbon wires before the DH test, see Fig. 8. The non-encapsulated cells exposed to soldering flux on the interconnected regions before the DH test (Group 3-d) showed the Type-2 failure mode after DH testing. There was a decrease in $EL_{LS,}$ but an increase in PL_{LS} intensities around the interconnected regions after 50 h of DH testing (100 °C, 85% RH), due to R_s increase, see Fig. 8 (a). Type-3 failure mode was realized in the non-encapsulated cells exposed to soldering flux between the interconnected regions prior to the DH test (Group 3-c). A significant drop in EL_{LS} but an increase in PL_{LS} intensities were seen in this cell due to an increase in R_s after DH testing, see Fig. 8 (b). The non-encapsulated cells exposed to acetic acid (35%) on the interconnected regions before DH testing showed Type-4 failure mode, see Fig. 8 (c). Both EL_{LS} and PL_{LS} intensities decreased in the interconnected regions due to increased recombination. Note that the line-like scratches seen in Fig. 8 (a) and (b) after DH testing were due to a sample breakage during manual handling and should be ignored. This result suggests that the Type-4 failure mode observed in the glass-backsheet modules with encapsulated HJT cells (Group 1) and cell precursors (Group 2-b) in this study is potentially due to the chemical reactions between acetic acid (hydrolyzed from EVA during DH testing) and moisture penetrating the module from the rear side (through the backsheet), resulting in recombination loss. The detail of how these reactions caused recombination to increase remains unclear; a more detailed study is required to fully understand this phenomenon.

The Type-2 and Type-3 failure modes observed in the glass-backsheet modules with encapsulated HJT cells (Group 1) and cell precursors (Group 2) presented in Figs. 4 and 5 are highly likely due to the involvement of soldering flux. These modules likely underwent different concentrations and/or types of soldering flux used for connecting busbars and ribbon wires than those of the mini-module that showed Type-1 and Type-4 failure modes after DH testing. Also, the soldering flux used for connecting ribbon/tabbing wires to busbars may be mixed with a high concentration of lead (Pb) and/or tin (Sn), and/or organic acid, which likely accelerates the chemical reaction between ribbon wires [Pb, copper (Cu), Sn)], silver paste (Ag), ITO layers (In, Sn), and moisture (H_2O) leading to corrosion in those regions [18,22–24]. The direct impact of flux and Pb solder in causing contact degradation after DH testing was also observed in other work where a different type of flux together with (or without) Pb solder used varied the extent of contact degradation (R_s increase) after DH testing [17]. It is essential to highlight that, in some cases, the usage of a different Ag paste also resulted in a Type-3 failure (data not shown). This was likely due to a high concentration of Cu (high corrosive elements) in these Ag pastes [25], which quickly interacted with moisture during the DH test, resulting in contact degradation. However, the Type-3 failure mode observed in our study was unlikely to be caused by only a reaction between the Ag metallization and moisture, as no Type-3 failure mode was realized in the non-encapsulated cell that directly underwent the DH test and/or was submerged entirely in water for up to 500 h (data not shown).

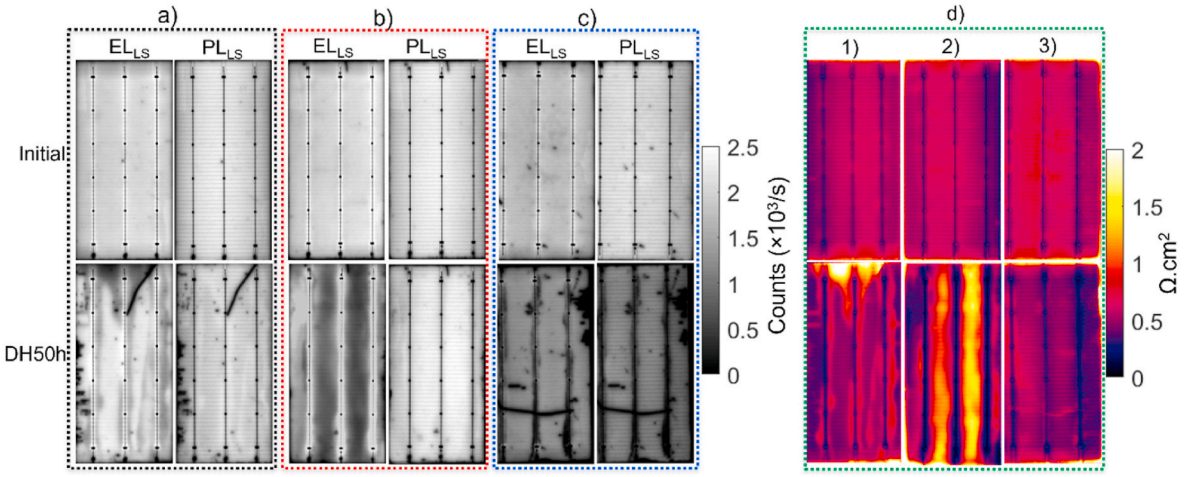

Fig. 8. Changes in EL_{LS}, PL_{LS} images of non-encapsulated cells with interconnected ribbon wires on both sides that pre-exposed to soldering flux a) on the interconnected regions (Group 3-d), b) between the interconnected regions (Group-3-c) and c) acetic acid (35%) on the interconnected regions (Group 3-e). d) change in R_s images of 1) Group 3-d, 2) Group 3-c, and 3) Group 3-e before and after 50 h of DH testing. These non-encapsulated cells show Type-2 (a), Type-3 (b), and Type-4 (c) failure modes after DH testing.

Furthermore, the silver paste used in this work did not contain any Cu additive.

It remains unclear why samples in Group 1 (mini-module with encapsulated cells) produced different results after DH testing as they were fabricated at industrial facilities. These mini-modules were all fabricated using the same HJT cell structure (same passivation, ITO, silver paste, and contact curing process), connected to the same type of ribbon/tabbing wires, and encapsulated with the same module structure (front glass, rear backsheet and EVA). However, these mini-modules were produced at different times. According to the DH testing results of non-encapsulated cells (samples in Group 3), it is highly likely that the samples in Group 1 were handled differently and/or underwent slightly different processes prior to encapsulation. Some mini-modules (those resulting in Type-1 failure mode after DH testing) might accidently be handled with contaminated gloves and/or placed on the contaminated stage during characterization and/or storage prior to the encapsulation, resulting in Type-1 failure mode after the DH test. Other mini-modules (those resulting in Type-2 and Type-3 failure modes after DH testing) likely underwent different concentrations and/or types of soldering flux used for connecting busbars and ribbon wires and/or somehow accidently contaminated with Pb and Sn prior to modules encapsulation; therefore, after DH testing, Type-2 and Type-3 appeared.

The mini-modules that resulted in Type-4 failure mode after the DH test were not likely to have been exposed to external contaminants (those that caused Type-1 failure mode). In addition, the soldering flux used for connecting the ribbon wires to busbars in these modules might be less or contain an insignificant amount of Pb/Sn and/or organic acid (note that these modules were fabricated at the same time as that of modules that showed Type-1 failure mode after DH testing). Therefore, after the DH test, Type-1, Type-2, and Type-3 failures were not detected in these mini-modules. The Type-4 failure mode observed in these modules highly likely only resulted from the byproduct of EVA (acetic acid) used for encapsulation.

Although the experimental design in this work cannot determine exactly how each failure mode occurred after DH testing, it demonstrates plausible situations that could happen in the industry environment and lead to the actual failure modes observed. This work clearly shows that HJT modules can exhibit a wide range of failure modes resulting from a complex interaction of the HJT solar cell with contaminants, soldering flux, moisture, and acidic acid, which may result in these modules failing their performance warranty. More work is needed to ensure that these failure modes are better understood and mitigated at the HJT solar cell level, as not all stressors can be avoided (e.g., moisture and acidic acid) at the module level.

It is also essential to note that although glass-glass modules (less susceptible to moisture ingress) rather than glass-backsheet modules are commonly used for HJT solar cells as studied in this work, it is likely that similar failure modes would occur in these modules, but over longer timescales. Therefore, these failure modes must be well understood and eliminated at preferably the solar cell level to ensure that HJT modules can meet their LCOE potential.

4. Conclusion

This work investigates damp heat-induced failure modes in the silicon HJT glass-backsheet modules. Four failure modes are identified after the DH test, and each failure mode requires different testing approaches to recreate the same failure signals at the cell level (non-encapsulated cells). Type-1 failure mode (point degradation) causes a P_{max} loss of up to ~40%$_{rel}$ after 4000 h of DH testing, with the primary loss due to the increasing localized recombination at the surface. This failure mode is potentially caused by chemical reactions between contamination (introduced to the cells during handling or characterization before encapsulation) and moisture, resulting in recombination loss after the DH test. Type-2 and Type-3 failure modes (degradation around and between interconnected regions of busbars and ribbon wires) caused P_{max} loss of ~5% and ~50%$_{rel}$ respectively. These failure modes are highly likely caused by the chemical reactions between moisture, soldering flux (or some contamination containing a high concentration of Pb), ribbon wires, Ag paste, and ITO layers, leading to corrosion on the failed regions and increased R_s. Type-4 failure mode (degradation at/on interconnected regions) causes a P_{max} loss of ~16%$_{rel}$ after 4000 h of DH testing. This failure mode is likely caused by a chemical reaction between acetic acid generated from EVA and water (penetrating the module from the rear side), leading to recombination loss. These results indicate that careful attention should be paid to all types of contamination when dealing with HJT solar cells, some of which are inherently present in module packing components. Hence, we suggest that the preferred solution is to mitigate these failure modes at the HJT solar cell level.

CRediT authorship contribution statement

Chandany Sen: Writing – review & editing, Writing – original draft, Validation, Methodology, Investigation, Formal analysis, Data curation, Conceptualization. **Haoran Wang:** Methodology, Investigation. **Xinyuan Wu:** Methodology, Investigation. **Muhammad Umair Khan:** Methodology, Investigation, Data curation. **Catherine Chan:** Writing – review & editing, Validation, Methodology. **Malcolm Abbott:** Writing – review & editing, Visualization, Validation, Supervision, Methodology, Investigation. **Bram Hoex:** Writing – review & editing, Validation, Supervision, Resources, Project administration, Funding acquisition, Conceptualization.

Declaration of competing interest

The authors declare that they have no known competing financial interests or personal relationships that could have appeared to influence the work reported in this paper.

Data availability

Data will be made available on request.

Acknowledgments

This work was supported by the Australian Government through the Australian Renewable Energy Agency (ARENA 1–060 Extension project). The responsibility for the views, information, or advice expressed herein is not accepted by the Australian Government. The authors also would like to thank Dr Alison Ciesla for her contributions in proofreading this manuscript to improve the clarity of the writing.

References

[1] I.M. Peters, J. Hauch, C. Brabec, P. Sinha, The value of stability in photovoltaics, Joule 5 (2021) 3137–3153, https://doi.org/10.1016/j.joule.2021.10.019.
[2] J. Tourino Jacobo, LONGi Sets 26.81% Efficiency Record for Heterojunction Solar Cells, 2022. Www.Pv-Tech.Org/, https://www.pv-tech.org/longi-sets-26-81-efficiency-record-for-heterojunction-solar-cells/. (Accessed 26 November 2022).
[3] J. Karas, A. Sinha, V.S.P. Buddha, F. Li, F. Moghadam, G. Tamizhmani, S. Bowden, A. Augusto, Damp heat induced degradation of silicon heterojunction solar cells with Cu-plated contacts, IEEE J. Photovoltaics 10 (2020) 153–158, https://doi.org/10.1109/JPHOTOV.2019.2941693.
[4] D. Adachi, T. Terashita, T. Uto, J.L. Hernández, K. Yamamoto, Effects of SiOx barrier layer prepared by plasma-enhanced chemical vapor deposition on improvement of long-term reliability and production cost for Cu-plated amorphous Si/crystalline Si heterojunction solar cells, Sol. Energy Mater. Sol. Cell. 163 (2017) 204–209, https://doi.org/10.1016/j.solmat.2016.12.029.
[5] H. Park, J.S. Jeong, E. Shin, S. Kim, J. Yi, A reliability study of silicon heterojunction photovoltaic modules exposed to damp heat testing, Microelectron. Eng. 216 (2019), 111081, https://doi.org/10.1016/j.mee.2019.111081.
[6] T. Ishii, A. Masuda, Annual degradation rates of recent crystalline silicon photovoltaic modules, Prog. Photovoltaics Res. Appl. 25 (2017) 953–967, https://doi.org/10.1002/pip.2903.

[7] M. Taguchi, J. Irikawa, M. Iwata, H. Kannou, Y. Murakami, S. Okamoto, Approaches to the long-term stability of silicon heterojunction modules, in: 4th International Workshop on Silicon Heterojunction Solar Cells, 2021.
[8] J.P. Singh, S. Guo, I.M. Peters, A.G. Aberle, T.M. Walsh, Comparison of glass/glass and glass/backsheet PV modules using bifacial silicon solar cells, IEEE J. Photovoltaics 5 (2015) 783–791, https://doi.org/10.1109/JPHOTOV.2015.2405756.
[9] SEMI PV79-0818, Test Method for Exposure Durability of Photovoltaic (PV) Cells to Acetic Acid Vapor, 2017.
[10] Y. Zhang, M. Kim, L. Wang, P. Verlinden, B. Hallam, Design considerations for multi-terawatt scale manufacturing of existing and future photovoltaic technologies: challenges and opportunities related to silver, indium and bismuth consumption, Energy Environ. Sci. 14 (2021) 5587–5610, https://doi.org/10.1039/d1ee01814k.
[11] D. Meza, A. Cruz, A.B. Morales-Vilches, L. Korte, B. Stannowski, Aluminum-doped zinc oxide as front electrode for rear emitter silicon heterojunction solar cells with high efficiency, Appl. Sci. (2019) 9, https://doi.org/10.3390/app9050862.
[12] M. Lokanc, R. Eggert, M. Redlinger, The Availability of Indium: the Present, Medium Term, and Long Term, National Renewable Energy Laboratory, 2015. www.nrel.gov/publications.
[13] M. Kasemann, L.M. Reindl, B. Michl, W. Warta, A. Schütt, J. Carstensen, Contactless qualitative series resistance imaging on solar cells, IEEE J. Photovoltaics 2 (2012) 181–183, https://doi.org/10.1109/JPHOTOV.2012.2184524.
[14] I. Zafirovska, M.K. Juhl, J.W. Weber, J. Wong, T. Trupke, Detection of finger interruptions in silicon solar cells using line scan photoluminescence imaging, IEEE J. Photovoltaics 7 (2017) 1496–1502, https://doi.org/10.1109/JPHOTOV.2017.2732220.
[15] I. Zafirovska, M.K. Juhl, T. Trupke, Comparison of line scan luminescence imaging techniques for defect characterisation in crystalline silicon solar modules, in: 2018 IEEE 7th World Conference on Photovoltaic Energy Conversion (WCPEC)(A Joint Conference of 45th IEEE PVSC, 28th PVSEC & 34th EU PVSEC), 2018, pp. 1364–1369.
[16] N. Kyranaki, Corrosion in Crystalline Silicon Photovoltaic Modules and the Influence on Performance, Doctoral Thesis, Loughborough University, 2020.
[17] Y. Ino, S. Asao, K. Shirasawa, H. Takato, Effect of soldering on the module degradation along bus bar in DH test and PCT for crystalline Si PV modules, in: 2018 IEEE 7th World Conference on Photovoltaic Energy Conversion (WCPEC)(A Joint Conference of 45th IEEE PVSC, 28th PVSEC & 34th EU PVSEC), 2018, pp. 3552–3557, https://doi.org/10.1109/PVSC.2018.8548219.
[18] N. Iqbal, D.J. Colvin, E.J. Schneller, T.S. Sakthivel, R. Ristau, B.D. Huey, B.X.J. Yu, J.N. Jaubert, A.J. Curran, M. Wang, S. Seal, R.H. French, K.O. Davis, Characterization of front contact degradation in monocrystalline and multicrystalline silicon photovoltaic modules following damp heat exposure, Sol. Energy Mater. Sol. Cell. (2022) 235, https://doi.org/10.1016/j.solmat.2021.111468.
[19] C. Camus, A. Adegbenro, J. Ermer, V. Suryaprakash, J. Hauch, C.J. Brabec, Influence of pre-existing damages on the degradation behavior of crystalline silicon photovoltaic modules, J. Renew. Sustain. Energy 10 (2018), https://doi.org/10.1063/1.5000294.
[20] K.R. Mcintosh, C.B. Honsberg, The Influence of Edge Recombination on a Solar Cell's Iv Curve, 2000. https://www.researchgate.net/publication/247910506.
[21] K.R. McIntosh, Lumps, Humps and Bumps: Three Detrimental Effects in the Current-Voltage Curve of Silicon Solar Cells, Doctoral Thesis, University of New South Wales, 2001.
[22] Y. Ino, S. Asao, K. Shirasawa, H. Takato, Investigation of degradation mode spreading interconnectors by pressure-cooker testing of photovoltaic cells, IEEE J. Photovoltaics 10 (2020) 188–196, https://doi.org/10.1109/JPHOTOV.2019.2950079.
[23] H. Conseil, M.S. Jellesen, V. Verdingovas, R. Ambat, Decomposition studies of no-clean solder flux systems in connection with corrosion reliability of electronics, InEuropean Corrosion Congress (Eurocorr), Estoril 1 (2013 Sep) 1–5.
[24] M.S. Jellesen, D. Minzari, U. Rathinavelu, P. Møller, R. Ambat, Investigation of electronic corrosion at device level, ECS Trans. 25 (30) (2010) 1–4.
[25] J. Karas, B. Phua, A. Mo, N. Iqbal, K. Davis, S. Bowden, A. Lennon, A. Augusto, Copper outdiffusion from copper-plated solar cell contacts during damp heat exposure, ACS Appl. Mater. Interfaces (2021), https://doi.org/10.1021/acsami.1c21218.